Nano Energy 129 (2024) 110076

Contents lists available at ScienceDirect

Nano Energy

journal homepage: www.elsevier.com/locate/nanoen

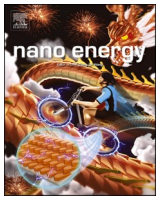

MOFs/MXene nano-hierarchical porous structures for efficient ion dynamics☆

Lixue Yang [a], Leo N.Y. Cao [a,b], Shaoxin Li [a,b], Puguang Peng [a,b], Han Qian [a,b], Gehan Amaratunga [c,d], Feiyao Yang [a], Zhong Lin Wang [a,e,*], Di Wei [a,f,*]

[a] Beijing Institute of Nanoenergy and Nanosystems, Chinese Academy of Sciences, Beijing 101400, China
[b] School of Nanoscience and Technology, University of Chinese Academy of Sciences, Beijing 100049, China
[c] Zhejiang University-University of Illinois at Urbana Champagne Institute (ZJUI) and School of Information Science and Electronics, Zhejiang University International Campus, Haining, China
[d] Electrical Engineering Division, Dept. of Engineering, University of Cambridge, Cambridge CB3 0FA, UK
[e] School of Materials Science and Engineering, Georgia Institute of Technology, Atlanta, GA 30332, USA
[f] Centre for Photonic Devices and Sensors, University of Cambridge, 9 JJ Thomson Avenue, Cambridge CB3 0FA, UK

ARTICLE INFO

Keywords:
Nano-hierarchical porous structures
1D MOFs
2D MXene
MOFs/MXene hybrid membranes
Osmotic power

ABSTRACT

Nature's various hierarchical structures exhibit exceptional performance in enhancing mass transport. However, how to bionic nano-hierarchical structures to enhance ion dynamics and achieve charge regulation is a significant challenge. Herein, a nano-hierarchical porous hybrid membrane inspired by nature was designed by integrating 1D metal-organic frameworks (MOFs) on the 2D MXene substrate utilizing MOF nanoparticles with tailorable positive and negative surface charges. The synergistic effects of the bioinspired nanohierarchical porous structure and surface charge interactions significantly enhance the performance and stability of the nanoconfined membrane, as corroborated by experimental characterizations and theoretical simulations. As a result, the optimized nanohierarchical porous membrane exhibits high a cation selectivity of 0.95, an outstanding power density of 35.04 W m^{-2}, and excellent stability over one month. Synergizing enhanced mass transport and ion dynamics in nano-hierarchically structured materials with tailored charge improves osmotic power generation efficiency and benefits logic circuits with controlled charge transport.

1. Introduction

In nature, hierarchically porous networks are evolved by natural selection and are pervasive in organismal systems, offering the distinct advantages of extremely high-efficiency mass transfer and exchange with minimum energy consumption [1]. A noteworthy example is found in the water transport system of plants, where a multi-scale pore structure containing roots, stems, and leaves optimizes flow conductance and enable an ideal photosynthesis rate [2]. The respiratory systems of insects, characterized by cuticle-lined tubes with highly branched structures throughout the body, also represent the natural porous networks. These structures minimize transfer the resistance of carbon dioxide (CO_2) and oxygen (O_2), enhancing their delivery within the body [3]. Additionally, hierarchical porous structures play crucial roles in the transmission of blood, odor, and nerve signals in the body, which also underscores their pivotal function in mass transfer [4–7]. Recognizing the significance of hierarchically porous structures, researchers have synthesized materials with similar characteristics, particularly in the fields of gas sensing and photocatalysis [8]. For instance, a macro-meso-microporous ZnO porous network was used to realize highly sensitive gas sensors utilizing the layer-by-layer evaporation method [1]. Meanwhile, biomimetic fiber membranes featuring nano-hierarchical porous structures were synthesized to enable ultrafast water transport and vapor diffusion [9]. Despite the myriad advantages and applications highlighted for nano-hierarchical porous structures, it has received little attention and has been overlooked in the realm of osmotic power generation.

☆ Prof Zhong Lin Wang, an author on this paper, is the Editor-in-Chief of Nano Energy, but he had no involvement in the peer review process used to assess this work submitted to Nano Energy. This paper was assessed, and the corresponding peer review managed by Professor Chenguo Hu, also an Associate Editor in Nano Energy

* Corresponding authors at: Beijing Institute of Nanoenergy and Nanosystems, Chinese Academy of Sciences, Beijing 101400, China.
E-mail addresses: zhong.wang@mse.gatech.edu (Z.L. Wang), dw344@cam.ac.uk (D. Wei).

https://doi.org/10.1016/j.nanoen.2024.110076
Received 29 June 2024; Received in revised form 26 July 2024; Accepted 30 July 2024
Available online 2 August 2024

Nanoconfined materials have attracted considerable attention recently for their prospects in osmotic power device applications [10]. For instance, one-dimensional (1D) nanoporous materials, such as metal-organic frameworks (MOFs), exhibit great potential in ion sieving and osmotic power, due to their adjustable pore sizes and tunable surface charges [11–13]. However, the scarcity of surface charge on MOFs have posed challenges to their independent film formation. Thus, they usually require a supporting film to achieve the necessary ion permeability in practical applications [14]. For example, a photo-responsive SP (spiropyrone)-MIL (Materials of Institut Lavoisier)-53 sub--nanochannel was constructed by integrating SP molecules into the MIL-53 framework on an anodic aluminum oxide (AAO) membrane, achieving an output power density of 8.3 $W m^{-2}$ under UV light [15]. Peng *et al.* composited a polystyrene suifonate (PSS)@MOF hybrid membrane using an electro-deposition method to incorporate PSS into MOF on AAO supporting film, yielding an output power density of 2.87 $W m^{-2}$ [16]. Xiao *et al.* proposed a heterogeneous membrane by coating self-assembled MOF monolayer (SAMM) film on UiO-66-NH_2 supporting film, realizing an output power density of 6.76 $W m^{-2}$ [17]. Despite many advancements, the aforementioned MOF membranes of the power densities remained low. On the other hand, two-dimensional (2D) nanomaterials, such as graphene oxide (GO) and MXene, offer avenues for improving the osmotic power [18–22]. They leverage advantages like reduced ion permeability distances due to thinner thickness and effective ion selectivity through the surface charge of functional groups [23,24]. Nevertheless, the power densities of most membranes reported so far were around 10 $W m^{-2}$ [25–27], but there still has a considerable gap between the theoretical energy conversion efficiency [28]. Therefore, it is crucial to develop a nano-confined membrane capable of achieving high osmotic power performance.

In this work, inspired by natural systems, the nano-hierarchical porous structure was constructed by 1D MOFs nanoparticles electrochemically modified onto 2D MXene nanosheets, realizing a high-performance osmotic power source. The thickness of the synthesized MIL −53-COOH/MXene hybrid membrane was a mere 4 μm, reducing the distance of ion permeability. Such a nano-hierarchical porous structure, coupled with the MOFs featuring abundant negative surface charges, synergistically elevated both ion permeability and cation selectivity. The MIL-53-COOH/MXene hybrid membrane exhibited impressive cation selectivity (t_n) of 0.95 and outstanding output power

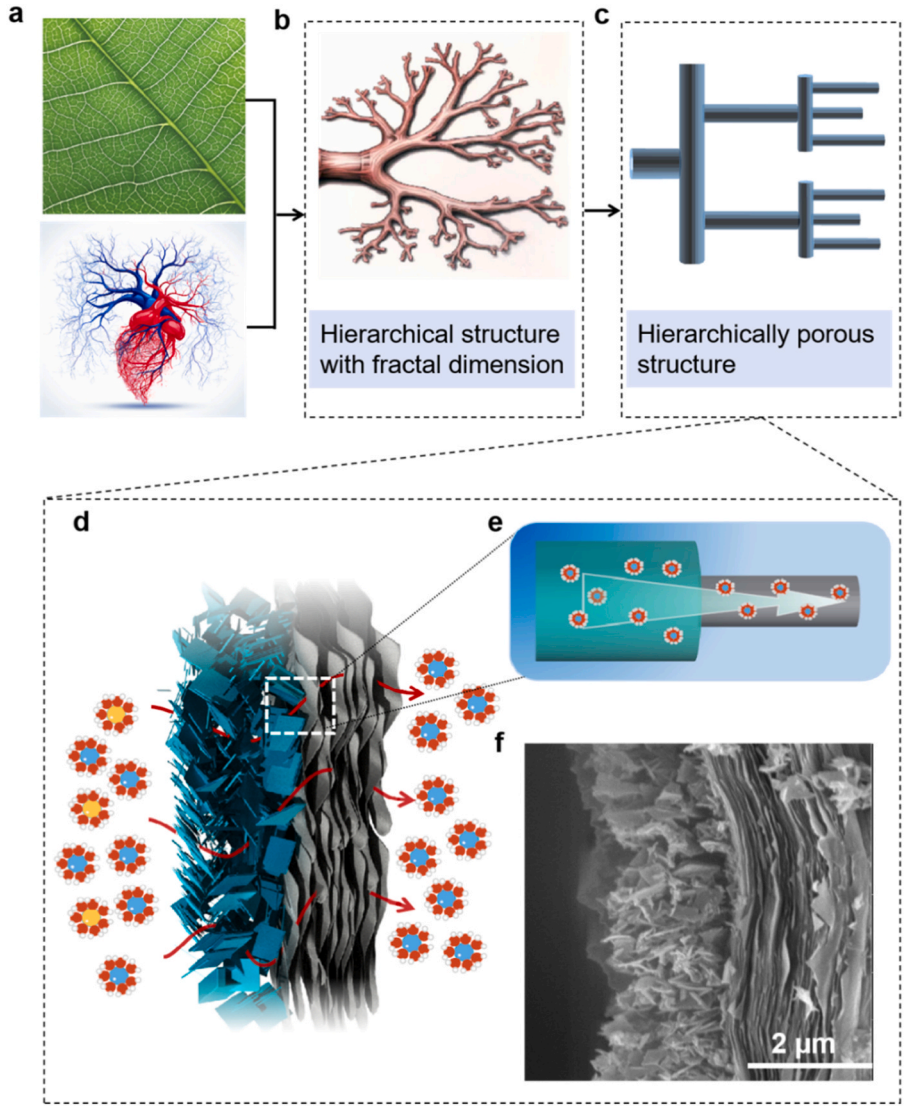

Fig. 1. Biological inspiration and ion transfer schematic of the nano-hierarchical porous membrane. (a) Hierarchical structures of leaf veins (top) and blood vessels (bottom) in biological organisms; (b) Hierarchical structure with fractal dimension from nature; (c) Bionic hierarchical porous structure model; Schematic illustration of ion transfer in (d) the MIL-53-COOH/MXene hybrid membrane, and (e) its enlarged image; (f) Cross-sectional SEM image of the MIL-53-COOH/MXene hybrid membrane.

density (35.04 W m^{-2}). More importantly, the MIL-53-COOH/MXene hybrid membrane showed excellent stability of power generation performance over one month, affirming its practicality. Distinctive attributes of various ions were scrutinized within MOFs possessing identical metal frame structures yet disparate surface charges. The results suggested that the MIL-53-COOH/MXene hybrid membrane, characterized by amounts of negative surface charges, exhibited superior osmotic power generation performance, in accordance with the Poisson-Nernst-Planck (PNP) simulation. In a word, by tailoring the surface charge of the hybrid membrane, the nano-hierarchical porous structure emerges as an effective strategy to provide a solution to the longstanding challenge of the osmotic power generation.

2. Results and discussion

2.1. Construction of nano-hierarchical porous structures

To facilitate ion transfer rates, biological organisms have developed hierarchical structures. For instance, in plants, leaf veins display an escalating number of branches that gradually narrow from macroscopic to microscopic scales, forming porous channels to optimize the energy conversion rate for photosynthesis [2]. Moreover, the structural complexity of vascular systems in living organisms mirrors a similar strategy to efficiently circulate substances like blood and nutrients (Fig. 1a) [6]. It could be seen from Fig. 1b that the structural model was inspired by those biological structures and featured hierarchically porous arrangements. This model incorporated a primary branch connected to numerous sub-branches (Fig. 1c), and such a biomimetic hierarchical structure with fractal dimension could enhance the efficiency of ion transfer. In this work, 1D MOF was integrated with 2D MXene nanosheets to synthesize the MIL-53-COOH/MXene hybrid membrane through electrodeposition process [29], which exhibited the hierarchical nanochannels. As shown in Fig. 1d, the nano-hierarchical porous membrane was composed of MIL-53-COOH diamond-shaped crystals and MXene membrane with nanoscale pores. The detailed preparation process of the hybrid membrane was provided in the supplementary information (Fig. S1). Due to an excessive MIL-53-COOH layer impeding ion transport, thereby reducing permeability. Conversely, an excessively thin MIL-53-COOH layer failed to achieve high ion selectivity. Therefore, the optimized electrodeposition was carried out under a current density of −0.89 A cm^{-2} for 5 min (Fig. S2). The design allowed ions to permeate through the MIL-53-COOH layer (as the first layer with an average size of 17.51 nm) and enter the MXene nanosheets (as the second layer with an average size of 4.34 nm), facilitating efficient ion transfer (ion selectivity and ion permeability). (Fig. 1e, Fig. S3). The scanning electron microscopy (SEM) image in Fig. 1f indicated that the thickness of the MIL-53-COOH/MXene hybrid membrane was approximately 4 μm, consisting of a ca. 2 μm-thick MIL-53-COOH layer with porous structures and a ca. 2 μm-thick MXene layer with a typical layered microstructure. The energy dispersive X-ray spectroscopy (EDX) mappings of the MIL-53-COOH/MXene hybrid membrane confirmed the presence of the elements Ti, C, O, and Al, indicating the successful synthesis of the hybrid membrane (Fig. S4).

Fourier transform infrared spectroscopy (FTIR) and Raman spectra were conducted to investigate the chemical properties of the MOF/MXene hybrid membranes. As confirmed in Fig. S5a, typical characteristic peaks of the –OH functional group in MXene, MIL-53-COOH/MXene, MIL-53/MXene and MIL-53-NH_2/MXene hybrid membranes were observed at approximately 3423 cm^{-1} [30–33]. The peaks at about 1643 cm^{-1}, 1439 cm^{-1} and 566 cm^{-1} were recognized as the C═O, C-O and Ti-O-Ti bonds, respectively. Additionally, the peaks at approximately 770 cm^{-1} and 673 cm^{-1} correspond to the Al-O bond, which were attributed to the functional groups of the organic ligands and the metal cluster in MIL-53-COOH, MIL-53 and MIL-53-NH_2 [30–33]. Raman spectroscopy results also confirmed the same findings (Fig. S5b). The region of 205–475 cm^{-1} represents in-plane vibrations of surface groups attached to Ti atoms, and the region between 580 cm^{-1} and 760 cm^{-1} is assigned chiefly to carbon vibrations. In addition, the peaks at approximately 570 cm^{-1} correspond to the Al-O bond, which were attributed to the functional groups of the organic ligands and the metal cluster in MIL-53-COOH, MIL-53, and MIL-53-NH_2 [30–32]. Through FTIR and Raman spectra analysis, there were no new covalent bonds formed between the MOF and MXene components of the hybrid membrane in our cases [30–32]. The interaction within the hybrid membrane via electrodeposition might primarily rely on electrostatic forces. Additionally, XRD analysis was employed to examine the crystal structures of both the top (MOF layer) and bottom (MXene layer) surfaces of the MIL-53-COOH/MXene hybrid membrane. As illustrated in Fig. S6, the diffraction peaks of the MIL-53-COOH/MXene hybrid membrane closely matched those of MIL-53-COOH nanocrystals across the 2θ range of 5°-25°. Notably, at 2θ≈6°, the characteristic diffraction peak of MXene was evident at the bottom layer of the MIL-53-COOH/MXene hybrid membrane [34,35]. As shown in Fig. S7, the interlayer spacing of the synthesized MIL-53-COOH/MXene hybrid membrane remained unchanged in the MXene layer [35]. These findings unequivocally confirmed the successful fabrication of the MIL-53-COOH/MXene hybrid membrane with nano-hierarchical porous structures.

In this work, the MIL-53-COOH was synthesized by an improved solvothermal method, and the detailed reaction processes were shown in Fig. S8 [30]. It could be seen from Fig. 2a that the MIL-53-COOH was composed of diamond-shaped morphology crystals. The X-ray diffraction (XRD) data demonstrated that MIL-53-COOH not only possessed the monoclinic crystal system (Fig. 2b) [33]. The EDX mapping confirmed the presence of C, O, and Al elements in the MIL-53-COOH (Fig. S9). Furthermore, its chemical bond compositions were also characterized by X-ray photoelectron spectroscopy (XPS). The C1s curve in Fig. 2c showed three different peaks at 293.68 eV, 289.68 eV, and 289.61 eV, corresponding to COOH, C-C, and benzene rings, respectively. Peaks for the O1s curve, appearing at 537.3 eV, signified the presence of OH groups (Fig. 2d). Peaks in the Al 2p curve at 79.79 eV was attributed to Al-O bonds, demonstrating the existence of Al metal centers in MIL-53-COOH crystals (Fig. 2e) [36]. The thermogravimetry analysis (TGA) in Fig. 2f demonstrated that the pores of the MIL-53-COOH were free of ligand molecules [37].

The detailed preparation process of MXene nanosheets was shown in Fig. S10 and those nanosheets were obtained through vacuum filtration on mixed cellulose esters (MCE) films (0.1 μm, 50 mm) [38]. The SEM image of MXene nanosheets revealed a typical layered structure, with the membrane thickness measuring only 2 μm, thus minimizing the permeability distance of ions (Fig. 2g). The XRD data in Fig. 2h highlighted the obvious characteristic peak (around 2θ=6.62°) of MXene membrane [35]. Additionally, the presence of C, O, and Ti elements was confirmed by the EDX mappings of MXene (Fig. S11). Furthermore, C-Ti-C, C-Ti-O, C-Ti-F, and C-Ti-(O, F) bonds were revealed by fitting the Ti 2p narrow scan in the XPS spectra (Fig. 2i). In the C 1 s spectrum, three peaks at 283 eV, 280.79 eV, and 283.17 eV corresponded to C-Ti, COO, and C-O, respectively (Fig. S12a). The peaks at 530.45 eV, 530.68 eV, and 528.2 eV in the high-resolution O 1 s spectrum were attributed to C═O, Ti-O, and C-O (Fig. S12b) [39], respectively, which further confirmed the successful synthesis of the MXene membrane.

2.2. Influencing factors on the ion dynamics in the ion selective membrane

The ion dynamic process across membranes is a crucial determinant in improving efficiency and performance in osmotic power. Utilizing the similar bulk mobility and hydration radii of K^+ and Cl^- ions, the ion-selective membrane was interposed between two reservoirs containing KCl solutions. As shown in Fig. 3a, both the MXene embrane and the MIL-53-COOH/MXene hybrid membrane exhibited linear Ohmic characteristics in the current-voltage (I-V) curves under the 0.01 M KCl solution [40]. It was noteworthy that the current of the MIL-53-COOH/MXene hybrid membrane was 3.48 times that of the

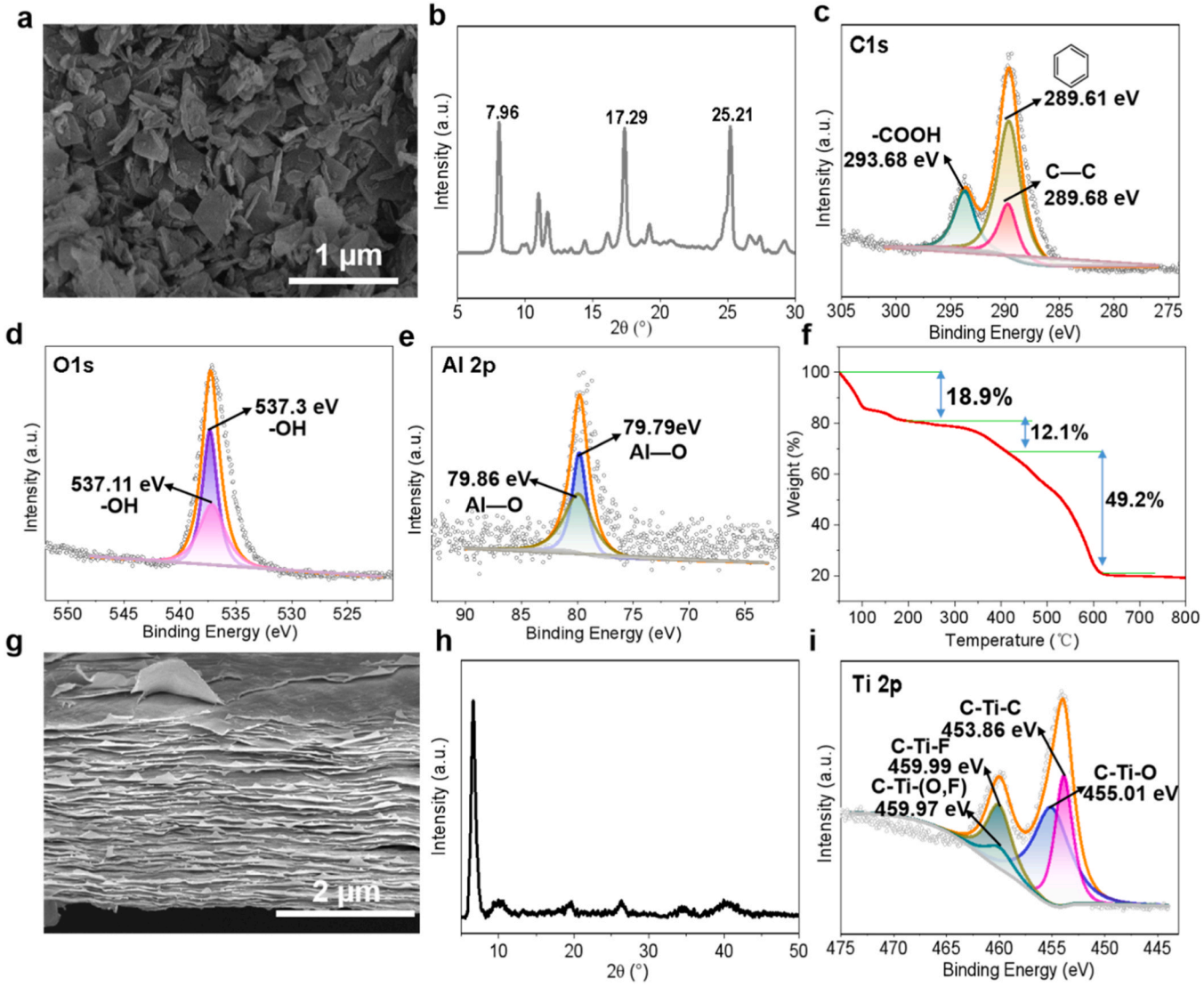

Fig. 2. Shape and nanostructure characterization of MIL-53-COOH crystals and the MXene membrane. (a) SEM image and (b) XRD of MIL-53-COOH nanocrystals; (c) C1 s, (d) O1 s, and (e) Al 2p XPS spectra of MIL-53-COOH nanocrystals; (f) TGA plot of MIL-53-COOH nanocrystals; (g) Cross-section SEM image of MXene membrane; (h) XRD and (i) Ti 2p XPS high-resolution spectra of pure MXene membrane.

pure MXene membrane, which indicated its superior ion permeability that might be due to the nano-hierarchical porous structure. Moreover, the trans-membrane conductance for both the pure MXene membrane and the MIL-53-COOH/MXene hybrid membrane evinced a pronounced dependency on the salinity gradient. It could be seen from Fig. 3b that their trans-membrane conductances both gradually diverged from the bulk value (marked as the black dashed line) with the decreasing in KCl solution concentration (from 10 M to 10^{-6} M) on one side, indicating the ion transfer behavior governed by the surface charge [41]. Similarly, the MIL-53-COOH/MXene hybrid membrane exhibited significantly higher conductance than the pure MXene membrane, with a maximum increase of nearly 59.41 times, exhibiting its much higher ion permeability. Under a 5-fold (0.01 M/0.05 M) NaCl salinity gradient, the t_n of the MIL-53-COOH/MXene hybrid membrane reached as high as 0.96, surpassing that of the pure MXene membrane. Even under 50-fold (0.01 M/0.5 M) and 500-fold (0.01 M/5 M) high NaCl salinity gradients where ion blocking phenomena were prone to occur [42], the t_n of the MIL-53-COOH/MXene hybrid membrane remained higher than that of the pure MXene membrane (Fig. 3c). Overall, the ion permeability and t_n of the MIL-53-COOH/MXene hybrid membrane showed superior performance, which might be attributed to its nano-hierarchical porous structure and the surface charge on the MIL-53-COOH nanocrystals.

Furthermore, the introduction of MIL-53-COOH endowed the hybrid membrane with ion sieving properties, since different metal ions possessed varying hydrated diameters. Fig. S13a showed the I-V curves of the MIL-53-COOH/MXene hybrid membrane in different electrolyte species (LiCl, NaCl, KCl, $CaCl_2$, and $MgCl_2$). Among the tested metal ions, K^+ exhibited the highest ion conductance, which might be due to its smallest hydrated radius (Table S1), enabling smooth transport across the channels. Additionally, as shown in Fig. S13b, the ion conductance order for the MIL-53-COOH/MXene hybrid membrane was $K^+ > Na^+ > Li^+ > Ca^{2+} > Mg^{2+}$. We further investigated the t_n order of the MIL-53-COOH/MXene hybrid membrane under different salinity gradient solutions. Under 5-fold (0.01 M/0.05 M), 50-fold (0.01 M/0.5 M), and 500-fold (0.01 M/5 M, KCl, saturation concentration) (Fig. S14) salinity gradients, the cation selectivity order of the MIL-53-COOH/MXene hybrid membrane remained $K^+ > Na^+ > Li^+ > Ca^{2+} > Mg^{2+}$, this trend was consistent with their ion conductance change. Therefore, the t_n of the MIL-53-COOH/MXene hybrid membrane in any salt solution surpassed that of the pure MXene membrane, indicating the great advantages of nano-hierarchical porous structures in osmotic power applications.

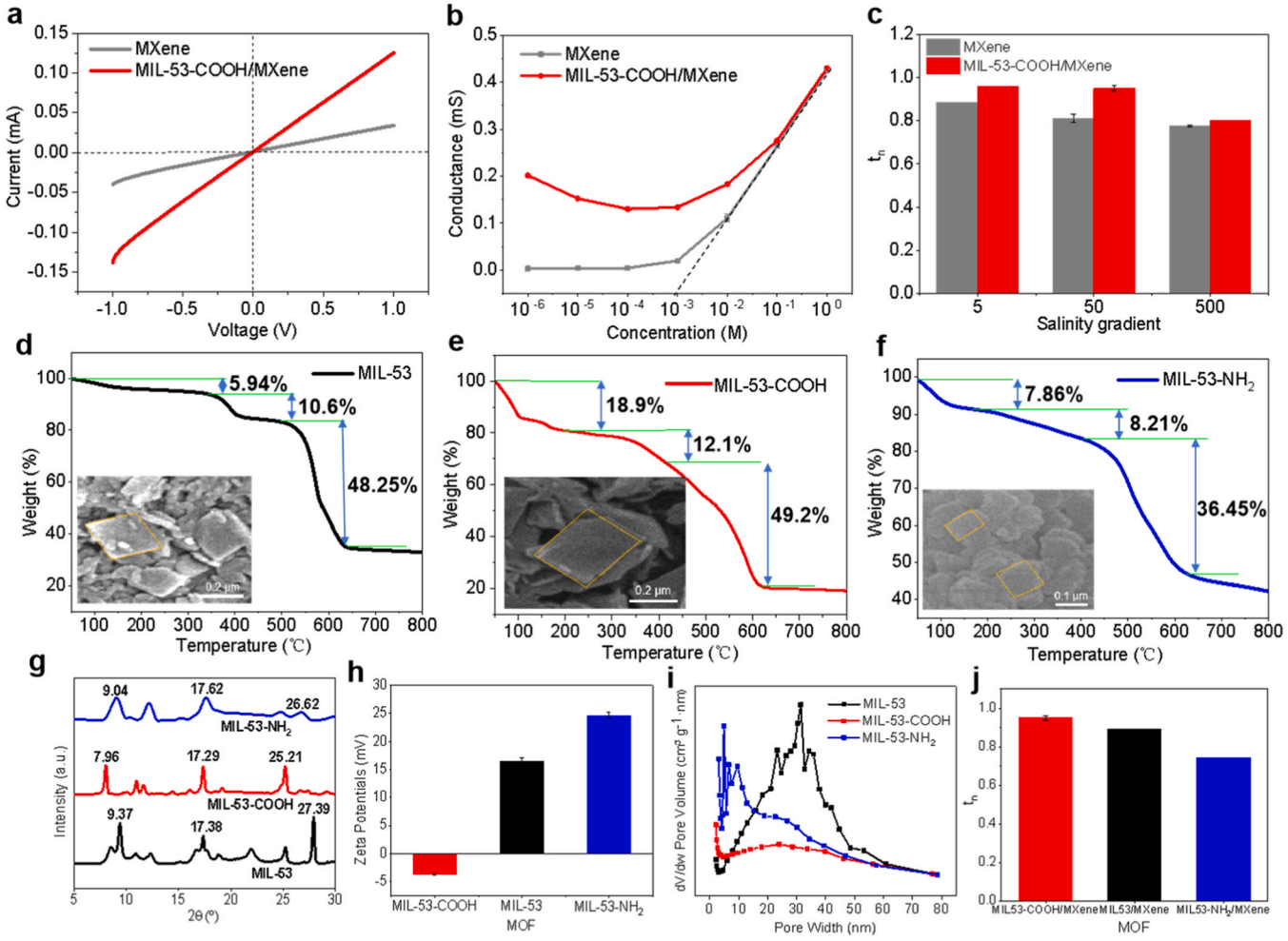

Fig. 3. Characteristics of different hybrid membranes with different surface charges (MIL-53/MXene, MIL-53-COOH/MXene, and MIL-53-NH_2/MXene). (a) I-V curvers of MXene membrane (gray line) and MIL-53-COOH/MXene hybrid membrane (red line) in 0.01 M KCl; (b) Ion conductance of MXene membrane (gray line) and MIL-53-COOH/MXene hybrid membrane (red line) under different salinity gradients of KCl solutions; (c) Ion selectivity (t_n) of MXene membrane (gray) and MIL-53-COOH/MXene hybrid membrane (red) under 5-fold, 50-fold, and 500-fold NaCl salinity gradients; TGA plot of (d) MIL-53 nanocrystals (insert: SEM image), (e) MIL-53-COOH nanocrystals (insert: SEM image), (f) MIL-53-NH_2 nanocrystals (insert: SEM image); Comparison of (g) XRD patterns, (h) Zeta potentials, (i) BET pore width analysis among MIL-53 nanocrystals (black), MIL-53-COOH nanocrystals (red), MIL-53-NH_2 nanocrystals (blue); (j) Comparison of cation selectivity (t_n) among MIL-53/MXene membrane (black), MIL-53-COOH/MXene membrane (red), MIL-53-NH_2 membrane (blue) under a 50-fold NaCl salinity gradient.

Surface charge and pore size are pivotal factors influencing ion dynamics in osmotic power. Here, three distinct MOFs (MIL-53, MIL-53-NH_2, and MIL-53-COOH) with varying surface charges were aggregated on MXene membranes to explore their impact on t_n. Detailed synthesis reaction processes of MIL-53 and MIL-53-NH_2 were provided in the Fig. S15 and S16 [15,43]. SEM images revealed that all three MOFs exhibited a diamond-shaped morphology (insert of Figs. 3d-3f). As shown in Figs. 3d-3f, the first weight loss corresponded to the removal of solvent molecules (e.g., water). The second weight loss represented the decomposition of weakly bound water within the framework pores and the partial decomposition of functional groups. Further decomposition of the framework occurs during the third weight loss. Additionally, the thermogravimetric analysis (TGA) confirmed the absence of ligand molecules within their pores [37]. Additionally, the XRD patterns showed that all three MOFs possessed nanocrystal structures, indicating their structural consistency within the narrow-pore MIL-53 framework [31,43]. It was noteworthy that the XRD peaks of the MIL-53-NH_2 nanocrystals were weaker and wider than the other two (Fig. 3g). Additionally, its binding energy as observed in the XPS spectra (Fig. S17 and S18) was the lowest [32]. These findings suggested the MIL-53-NH_2 nanocrystals had smaller crystal particles, which potentially contributed to their stronger electrostatic force and shorter bond length. Synthesized MIL-53, MIL-53-COOH, MIL-53-NH_2 nanocrystals and MXene exhibited Zeta potentials of 16.48 mV, −3.71 mV, 24.62 mV, and −47.15 mV, respectively (Fig. 3h, Table S2). Surface charge density calculations under neutral conditions yielded values of 3.7 mC m^{-2}, −1 mC m^{-2}, 5.6 mC m^{-2} and −10.59 mC m^{-2} for MIL-53, MIL-53-COOH, MIL-53-NH_2, and MXene (Table S2). This indicated MIL-53-COOH and MXene carried negative surface charges, both the MIL-53/MXene and MIL-53-NH_2/MXene hybrid membranes carried positive surface charges, with the latter exhibiting higher positive surface charges. The Brunauer-Emmett-Teller (BET) average pore size distribution curves showed the mean aperture sizes followed the order MIL-53 (19.28 nm) > MIL-53-COOH (17.51 nm) > MIL-53-NH_2 (10.55 nm) (Fig. 3i). More importantly, the pore sizes of MIL-53-COOH were more uniform. Under a 50-fold NaCl salinity gradient, the observed order of t_n for the three MOFs was MIL-53-COOH/MXene > MIL-53/MXene > MIL-53-NH_2/MXene (Fig. 3j). This underscores the influence of surface charge on the t_n of the ion-selectivity membranes. The MIL-53-COOH/MXene hybrid membrane, characterized by negative surface charges, exhibited superior cation selectivity.

2.3. Poisson-Nernst-Planck simulation on cation selectivity

The t_n feature of the hybrid membrane was further investigated by Poisson-Nernst-Planck (PNP) analysis [44]. In the simulation, the hybrid membrane was modeled as a seven-pore system (Fig. S19), considering its porous structure. The final negative surface charges on the MIL-53-COOH/MXene hybrid membrane implied its significant cation selectivity. The concentration distribution of K^+ and Cl^- surrounding the pores resulted in the establishment of an electrostatic potential along the salinity gradient direction. Due to the inherent negative charge on the membrane surface, cations were allowed to pass through efficiently. As illustrated in Fig. 4a, b, the transference rate of K^+ cations through the MIL-53-COOH/MXene hybrid membrane reached 90 %, markedly higher than that of Cl^- anions (36 %). In contrast, the MIL-53/MXene and MIL-53-NH_2/MXene hybrid membranes possessed positive surface charges, thus the transport of hydrated K^+ ions across MIL-53/MXene membranes were only 23.5 %, and further reduced to 6.9 % after modifying the positively charged amino group on the MIL-53/MXene membranes (Fig. 4c, d). Consequently, the order of t_n among the hybrid membranes followed as MIL-53-COOH/MXene > MIL-53/MXene > MIL-53-NH_2/MXene, consistent with the experimental results (Fig. 3j).

Besides, time-dependent ion concentration was investigated by a time-dependent PNP model to unveil more details about the t_n of the MIL-53-COOH/MXene hybrid membrane. Specifically, the top boundary of K^+ ions infiltrated the membrane region considerably faster than Cl^-, because the latter suffered steric effects from the negative surface charges of the MIL-53-COOH/MXene hybrid membrane. Thus, the concentration of K^+ ions near the MIL-53-COOH/MXene hybrid membrane region remained significantly higher than that of Cl^- throughout the time simulation (Fig. S20), due to its negative surface charge and the smaller hydrated diameter of K^+ ions.

Furthermore, the simulation extended to various cations with distinct hydrated diameters, including Na^+, Li^+, Ca^{2+}, and Mg^{2+}, to assess their transport rates within the MIL-53-COOH/MXene hybrid membrane under a 50-fold salinity gradient. The stimulated results of ion transport rate followed the order of $K^+ > Na^+ > Li^+ > Ca^{2+} > Mg^{2+}$ (Figs. 4e-4h), closely aligned with the comparison of hydrated diameters, and exhibited good congruence with the experimental results (Fig. S13a). This observation can be attributed to the formation of hydrated ions in salt solutions, wherein the hydrated diameter of metal cations falls within the range of 6.5–9.0 *Å* (Table S1). Larger hydrated diameters pose a greater challenge for trans-membrane transport. Consequently, divalent cations, characterized by a larger hydrated diameter, faced increased shielding, while monovalent cations with a smaller hydrated diameter could transport the channels more smoothly. As a result, the K^+ exhibited the highest ion conductance within the MIL-53-COOH/MXene, among those various electrolyte solutions (Fig. S13b).

2.4. Osmotic power harvesting

The MIL-53-COOH and MXene components of the hybrid membrane both possess negative charges in neutral solutions. Applying a salinity gradient across the MIL-53-COOH/MXene hybrid membrane induces a net flux of cations, thereby generating a diffusion potential (V_{diff}). Fig. S21 depicted I-V and t_n of MIL-53-COOH/MXene under 50-fold NaCl salinity gradients in opposing configurations. When the MXene side of the hybrid membrane faced the high-concentration electrolyte, the membrane's selectivity notably decreased, with t_n values of 0.66 at a 50-fold salinity gradient. Conversely, when the MOF (MIL-53-COOH) side was exposed to the high-concentration electrolyte, the membrane's selectivity significantly increased. As illustrated in Fig. S21b, the t_n values were 0.95 at 50-fold salinity gradients. Thus, these findings underscore that the MIL-53-COOH side of the hybrid membrane serves as the preferred direction for osmotic power, aligning with previous reports on cation selectivity in heterogeneous membranes [45].

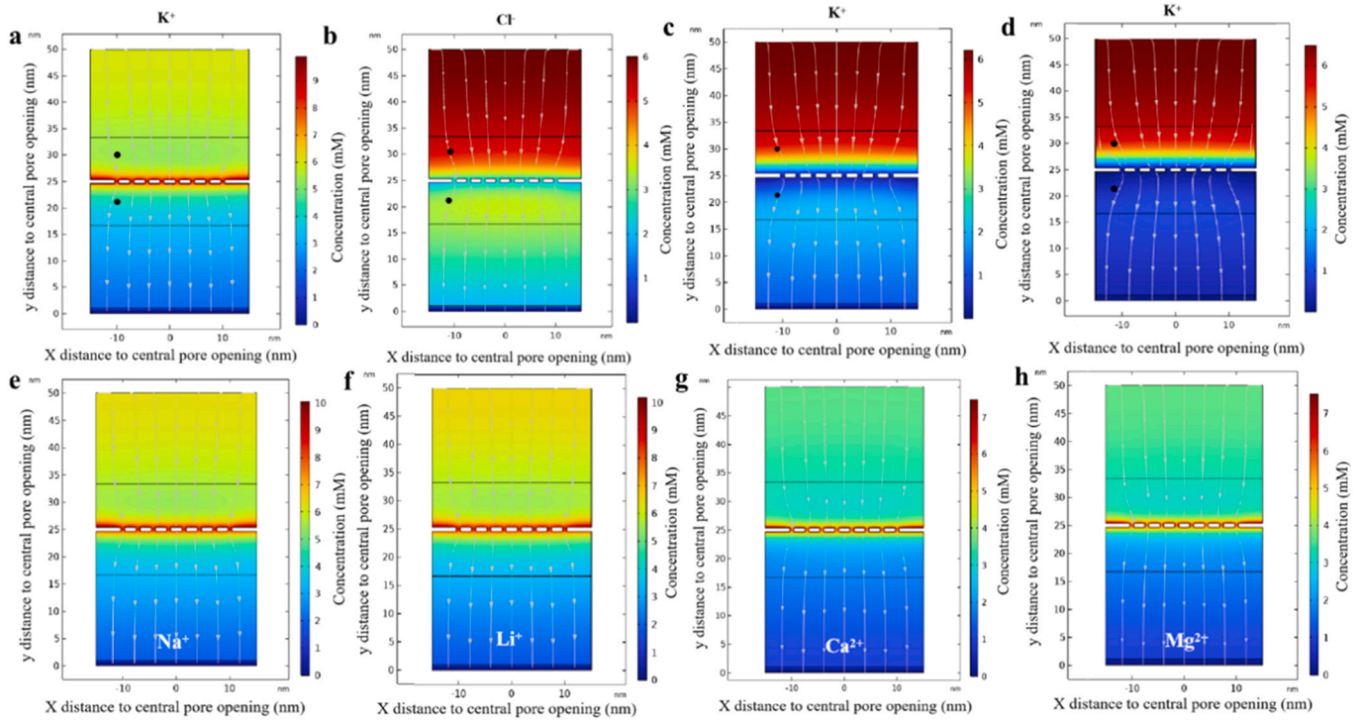

Fig. 4. Ion selectivity simulation. Steady-state concentration distribution of (a) K^+ and (b) Cl^- near MIL-53-COOH/MXene hybrid membrane with a surface charge density of -1 mC m^{-2} (-3.7 mV); Steady-state concentration distribution of K^+ near (c) MIL-53/MXene hybrid membrane and (d) MIL-53-NH_2/MXene hybrid membrane with surface charge densities of 3.7 mC m^{-2} (17.38 mV) and 5.6 mC m^{-2} (25.06 mV); Steady-state concentration diatribution of (e) Na^+, (f) Li^+, (g) Ca^{2+}, (h) Mg^{2+} near MIL-53-COOH/MXene hybrid membrane with a surface charge density of -1 mC m^{-2} (-3.7 mV). The top concentration was 10 mM, and the bottom concentration was 0 mM.

The ion transport and osmotic power conversion properties of homogeneous membranes of MIL-53-COOH, MIL-53, and MIL-53-NH_2 were also examined. Due to the difficulty of MOF film formation alone [29], MOF homogeneous membranes were prepared on the positively charged anodic aluminum oxide (AAO) substrate. As depicted in Fig. S22, at a 50-fold KCl salinity gradient, the absolute t_n value of MIL-53-COOH, MIL-53, and MIL-53-NH_2 homogeneous membranes was approximately 0.52, a value notably lower than that of MOF/MXene hybrid membranes. Similarly, the power densities of MOF homogeneous membranes were found to be less than 1 W m^{-2}, significantly lower compared to MOF/MXene hybrid membranes. It was worth noting that, since both MIL-53, MIL-53-NH_2, and AAO were positively charged, the MIL-53 and MIL-53-NH_2 homogeneous membranes carry a positive charge, demonstrating anion selectivity. The inferior results of both t_n value and power density from the MOF alone emphasize the crucial role of the nano-hierarchical porous structure formed by MOF/MXene in enhancing osmotic power conversion efficiency.

Benefiting from the remarkable permselectivity of the MIL-53-COOH/MXene hybrid membrane, a comprehensive evaluation of its osmotic power conversion capabilities was conducted using the experimental device (Fig. 5a). Here, the solution concentration was fixed at 0.01 M NaCl on the MXene side, while it varies from 0.05 to 5 M NaCl on the MIL-53-COOH side. The results showed that under three different salinity gradients, the ion current was positively correlated with the applied voltage, and both V_{diff} and I_{sc} increased with the increase in salinity gradients (Fig. S23a, Table S3). The MIL-53-COOH/MXene hybrid membrane exhibited energy conversion efficiencies (η) of 46 %, 45 %, and 30.12 %, respectively, under NaCl solutions with different salinity gradients of 5-fold, 50-fold, and 500-fold (Fig. S23b). The practical utilization of harvested osmotic power was assessed by connecting it to an external circuit with an electric load (R_L). We investigated the output current density and power density of the MIL-53-COOH/MXene hybrid membrane as a function of the external load resistance under various 5-fold, 50-fold and 500-fold salinity gradients. The current density decreases with increasing resistance (Fig. 5b), leading to a local maximum in power density when the external resistance matches the internal resistance of the membrane [46]. As depicted in Fig. 5c, the maximum output power densities were approximately 10.71 W m^{-2}, and 35.04 W m^{-2} under the 50-fold and 500-fold NaCl salinity gradients, respectively, much higher than the MXene membrane (Fig. S24). The power generation efficiencies of the MIL-53-COOH/MXene hybrid membrane were evaluated in addition to NaCl salinity solution, across a 500-fold salinity gradient (0.01 M/5 M) of LiCl, $CaCl_2$, $MgCl_2$, and KCl (saturation concentration), yielding power densities of 18.96 W m^{-2}, 17.52 W m^{-2}, 9.78 W m^{-2}, and 48.22 W m^{-2}, respectively (Fig. S25). The above results indicated the great advantages of nano-hierarchical porous structures in osmotic power applications.

For comparison, MIL-53/MXene and MIL-53-NH_2/MXene hybrids were also tested under a 50-fold salinity gradient, as illustrated in Fig. S26. The MIL-53/MXene hybrid membrane exhibited η and power density values of 40.6 % and 9.75 W m^{-2} under a 50-KCl salinity gradient, and 39.3 % and 2.21 W m^{-2} under a 50-fold NaCl salinity gradient, respectively. The MIL-53-NH_2/MXene hybrid membrane displayed η and power density values of 30.8 % and 1.9 W m^{-2} under a 50-fold KCl salinity gradient, and 24.37 % and 0.89 W m^{-2} under a 50-fold NaCl salinity gradient, respectively. More importantly, the output power density of the MIL-53-COOH/MXene hybrid membrane displayed no discernible attenuation at a 500-fold salinity gradient over a month (Fig. 5d), which indicated its stable performance for practical application. In summary, among the reported osmotic power harvesting systems to date, it is noteworthy that the MIL-53-COOH/MXene nano-

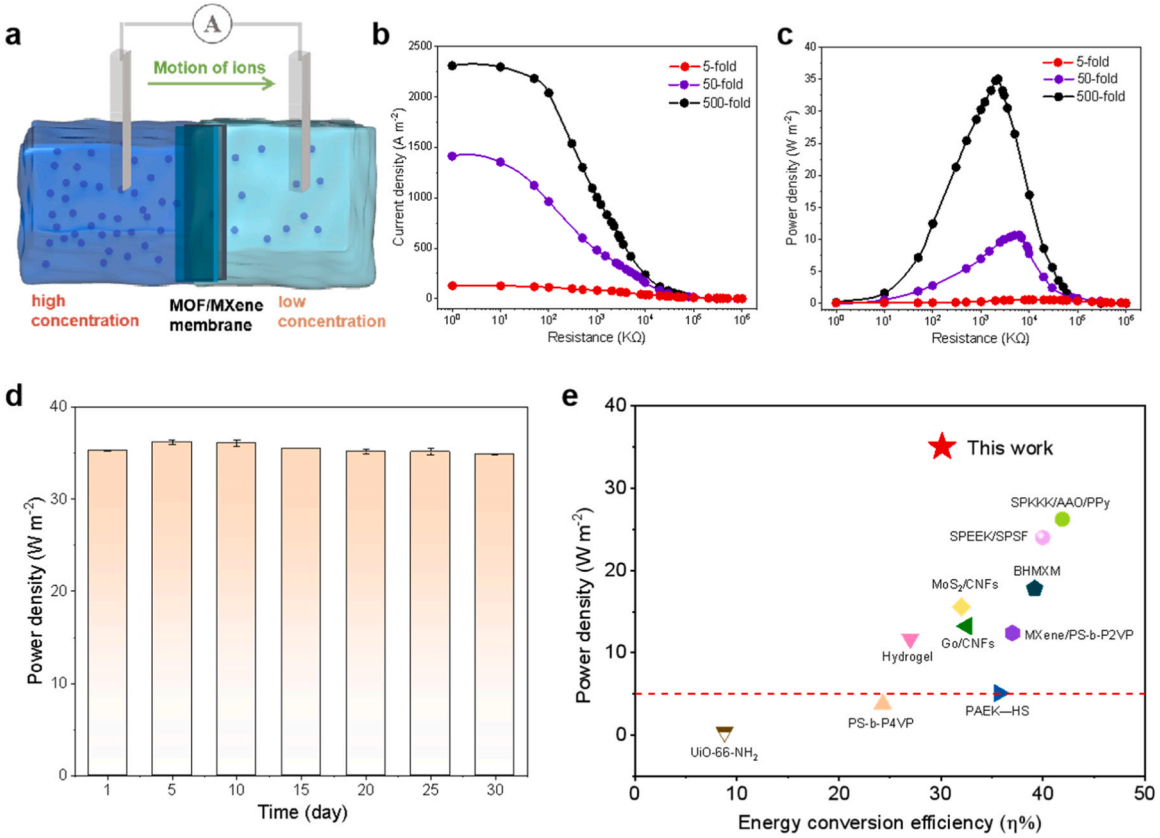

Fig. 5. Osmotic power conversion properties. (a) Schematic of the osmotic power conversion process; (b) Current density and (c) power density of the MIL-53-COOH/MXene hybrid membrane under different NaCl salinity gradients; (d) The stability of the MIL-53-COOH/MXene hybrid membrane in harvesting the osmotic power at a 500-fold salinity gradient; (e) Comparison of power density and η of the MIL-53-COOH/MXene hybrid membrane and other reported membranes.

hierarchical porous structure achieved an unprecedented output power density (Fig. 5e, Table S4).

3. Conclusion

In summary, we employed a straightforward electrodeposition strategy to synthesize three hybrid membranes with nano-hierarchical porous structures, each characterized by a distinct surface charge. Among these, the MIL-53-COOH/MXene hybrid membrane, modified with negative surface charges, demonstrated unparalleled cation selectivity and was the most efficient in osmotic power harvesting. This superiority might be attributed to the robust synergistic effect between the negative surface charges on MIL-53-COOH and the nano-hierarchical porous structure of the hybrid membrane. PNP analysis indicated the cation selectivity of the hybrid membrane could be regulated by its surface charge. Specifically, the specific pore sizes of MIL-53-COOH, coupled with the classically structured MXene, significantly contributed to enhanced cation selectivity within the nano-channels, facilitating cation permeation. The osmotic device with the MIL-53-COOH/MXene hybrid membrane achieved an impressive cation selectivity of 0.95, and an output power density of 35.04 W m^{-2}. Furthermore, the output power of the MIL-53-COOH/MXene hybrid membrane showed no significant decrease over one month, exhibiting remarkable stability in practical application. Through the modulation of surface charge within the nano-channels and the implementation of structural design, we anticipate that various hybrid membrane channels featuring nano-hierarchical porous structures will propel the application of osmotic power conversion as well as in domains such as gas separation, ion sieving, and seawater desalination.

4. Experimental section

4.1. Chemicals and materials

Aluminum chloride hexahydrate ($AlCl_3{\cdot}6\ H_2O$, 97 %), 1,2,4-terephthalic acid (H_3BDC, 98 %), terephthalic acid (H_2BDC, 99 %), 2-amino-terephthalic acid (BDC-NH_2, 98 %), tetrabutylammonium hexafluorophosphate ($(NBu_4)PF_6$, 98 %), Sodium hydroxide (NaOH, 97 %), Potassium chloride (KCl, 99.5 %), Sodium chloride (NaCl, 99.5 %), Lithium chloride (LiCl, 99 %), Calcium chloride ($CaCl_2$, 94 %), Magnesium chloride ($MgCl_2$, 99 %), Lithium fluoride (LiF, 99 %), N, N-dimethylformamide (DMF, 99.5 %) and titanium aluminum carbide (Ti_3AlC_2, 98 %) were purchased from Macklin. Hydrochloric acid (HCl, 37 %) was purchased from Beijing Chemical Plant Co., Ltd. Methyl alcohol (CH_3OH, 99.5 %) and was purchased from Shanghai Titan Scientific Co., Ltd. Mixed cellulose esters (MCE) films (0.1 μm, 50 mm) were purchased from Haiyan New Oriental Plastic Technology Co. Ltd. All water solutions were prepared in Milli-Q water (18.2 MΩ).

4.2. Preparation of the MIL-53-COOH nanocrystals

The MIL-53-COOH nanocrystals were synthesized using a ligand-salt induced strategy based on a solvothermal method [31]. First, about 690 mg of NaOH was dissolved in 10 ml of deionized water and cooled to room temperature. Thereafter, 1.4 g of H_3BDC was added to the above solution, ensuring it was completely dissolved through continuous agitation. 2.42 g of $AlCl_3{\cdot}6\ H_2O$ was dissolved in an additional 10 ml of deionized water to achieve a homogeneous solution. The above two solutions were mixed and stirred for 15 minutes, followed by transferring the mixture to a PTFE reactor and heating it at 100 ℃ for 48 h. The resultant white precipitate was isolated via centrifugation, washed with deionized water and methanol, and ultimately desiccated at 80 ℃ for 12 h. The synthesized MIL-53-COOH was characterized by the absence of excess organic ligands in its pores.

For comparison, MIL-53 nanocrystals were synthesized using the same method, but H_2BDC was added to the NaOH solution [41]. To investigate the surface charge and pore size of the nano-hierarchical porous structures of MIL-53, MIL-53-COOH, and MIL-53-NH_2 nanocrystals, MIL-53-NH_2 was synthesized by the traditional solvothermal method [16]. In brief, 760 mg of $AlCl_3{\cdot}6\ H_2O$ and 560 mg of BDC-NH_2 were solubilized in 30 ml of DMF and transferred to a PTFE reactor at 150 ℃ for 24 h. Centrifuge the mixture to obtain the yellow precipitate, which was then immersed in DMF for an additional 24 h, cleansed with methanol, and dried at 80 ℃ for 12 h. The synthesized MIL-53-NH_2 similarly had no excess organic ligands in its pores.

4.3. Preparation of the negatively charged MXene membrane

The MXene membrane was synthesized employing a vacuum filtration-assisted method [35]. First, 1.6 g of LiF was dissolved in 20 ml of HCl. Subsequently, 1 g of Ti_3AlC_2 was added to the above solution and stirred continuously for 24 h at 48 °C. Centrifuge the mixture and collect the precipitation, then wash it twice with 1 M HCl, followed by washing with deionized water to pH≈6 to obtain MXene precipitate. After that, a certain amount of MXene precipitate was deposited on an MCE membrane (with a pore size of 0.1 μm and a diameter of 50 mm) for vacuum filtration to obtain an MXene membrane, which was then dried at 40 ℃.

4.4. Fabrication of the MIL-53-COOH/MXene hybrid membrane

The MIL-53-COOH/MXene hybrid membrane was synthesized by a simple electrodeposition strategy [30]. Initially, a designated proportion of MIL-53-COOH was dispersed in 20 ml of methanol, while 10 mg of $(NBu_4)PF_6$ was dissolved in 30 ml of methanol, with stirring continuing until complete dissolution. The electrochemical system consisted of a platinum wire counter electrode, an Ag/AgCl reference electrode, and a specific size of MXene film as the working electrode in the aforementioned solution. An electrodeposition process was conducted at ambient temperature, applying a current density of -0.89 mA cm^{-2} for 5 minutes to obtain MIL-53-COOH/MXene hybrid film. Finally, the hybrid membrane was washed with methanol, followed by vacuum drying at 40 ℃ for 12 h. MIL-53/MXene and MIL-53-NH_2/MXene hybrid membranes were synthesized by the same procedure.

4.5. Characterization and measurements

A field emission scanning electron microscope (FEI/Nova NanoSEM450) was used to observe the surface and sectional morphology of the MIL-53, MIL-53-COOH, MIL-53-NH_2 nanocrystals, MXene membrane, and MIL-53-COOH/MXene hybrid membrane. Energy dispersive X-ray spectroscopy (EDX) was used to delineate the element distribution of the MIL-53-COOH nanocrystals, MXene membrane, and MIL-53-COOH/MXene hybrid membrane. X-ray diffraction (XRD, Xpert3 Powder) with a Cu Kα radiation source (40 KV and 40 mA) was used to elucidate the crystalline structures inherent to the MIL-53-COOH, MIL-53, MIL-53-NH_2 nanocrystals, and MXene membrane. A near atmospheric pressure X-ray photoelectron spectrometer (NAP-XPS, SPECS, Germany) was employed to ascertain the elemental composition and the chemical states of the elements present in the MIL-53-COOH, MIL-53, and MIL-53-NH_2 nanocrystals and MXene membrane. To determine the zeta potential values, the MIL-53-COOH, MIL-53, and MIL-53-NH_2 nanocrystals were analyzed using a zeta potential analysis system (BeNano Zeta) at 298k. The pore size distribution of the MIL-53 nanocrystals, MIL-53-COOH nanocrystals, and MIL-53-NH_2 nanocrystals, and the MXene membrane were characterized using a Micromeritics 3 Flex gas sorption analyzer. The MIL-53, MIL-53-COOH, and MIL-53-NH_2 nanocrystals were degassed at 180 ℃ for 48 h before each measurement. The MXene membrane was degassed at 40 ℃ for 48 h before each measurement. TGA (Mettler Toledo LLC., OH, Switzerland) was used to record the TGA curves of MIL-53, MIL-53-COOH, and MIL-53-NH_2 nanocrystals at 50 ℃ and 800 ℃.

4.6. Electrical measurements

A multichannel chemical workstation (Multi Autolab M204) was used to record the ion current through the ion-selective membrane. A standard Ag/AgCl reference electrode was used to accurately assess the current-voltage (I-V) curves and calculate the output power density. The reference electrode serves as a stable, known reference point for potential measurements during the electrochemical process. The hybrid membranes were sandwiched in two electrolytic cells containing an electrolyte solution. This configuration ensures that the hybrid membranes were exposed to the electrolyte, allowing for the ion transport that was being measured. The effective test area is specified to have an area of roughly 0.03 mm^2. This dimension is critical for quantifying the current in the area of the membrane. The voltage applied across the membrane during these measurements spans a range of −1 V to 1 V.

The energy conversion efficiency (η) was calculated by the equation as follows:

$$\eta = (2t_n - 1) \times 100\%$$

t_n was the cation transference number, which can be calculated as:

$$t_n = \frac{1}{2}\left[\frac{\varepsilon}{\frac{RT}{F}\ln\frac{\partial_H}{\partial_L}} + 1\right]$$

where ε, R, T, F, α_H, and α_L referred to the membrane potential, gas constant, absolute temperature, Faraday constant, high concentration, and low concentration, respectively.

The surface charge density (σ) was calculated by the following equation:

$$\sigma = \frac{\varepsilon_r \varepsilon_0 \xi}{\lambda_{Deb}}$$

Where ε_r, ε_0, ξ, and λ_{Deb} represent the permittivity of water, the permittivity of vacuum, Zeta potential, and Debye length, respectively. The Debye length was calculated using the following equation:

$$\lambda_{Deb} = \sqrt{\frac{\varepsilon_r \varepsilon_0 RT}{2cz^2F}}$$

Where ε_r, ε_0, R, T, c, z, and F represented the permittivity of water, the permittivity of vacuum, the gas constant, the absolute temperature, the concentration of the solution, the valence number, and the Faraday's constant.

4.7. Stability testing of the MIL-53-COOH/MXene hybrid membrane

The MIL-53-COOH/MXene hybrid membrane was sandwiched in two electrolytic cells containing different salinity gradients (0.01 M/5 M NaCl). Measurements of the output power density were conducted at consistent intervals within a controlled experimental environment. The MIL-53-COOH/MXene hybrid membrane remained perpetually submerged in the assay solution, with periodic replacement of the electrolytes preceding each power density measurement.

4.8. The PNP model

Ion transport across the MIL-53-COOH hybrid membrane had been computationally simulated via the coupled Poisson-Nernst-Planck (PNP) equations. The total flux of each ion species, denoted as J_i, can be expressed with a Fickian diffusion term, which accounts for concentration-driven migration, and a drift term, which describes the movement of ions under an electric field.

$$J_i = -D_i \nabla c_i - u_{m,i} z_i F c_i \nabla \phi$$

$$u_{m,i} = \frac{D_i}{K_B T}$$

where index i corresponds to the ith ion species, Di, ci, and zi are the diffusion coefficient, ion concentration, and valence of species i, respectively, um,i is the mobility, F is the Faraday constant, ϕ is the electrostatic potential, K_B is the Boltzmann constant, and T is the absolute temperature.

The electrostatic potential is contingent upon localized charges affixed to the interface of the membrane, while the emergent mobile charges stem from spatially varying ion concentrations, as delineated by the Poisson equation：

$$-\nabla \bullet (\varepsilon \varepsilon_0 \nabla \phi) = \sum_i z_i e c_i$$

$$n \bullet (\varepsilon \varepsilon_0 \nabla \phi) = \sigma_s$$

where ε_0 is the vacuum dielectric constant, ε is the relative dielectric constant of the aqueous solution, σ_s is the surface charge density of the membrane, and n is the unit normal vector, pointing outwards to the membrane surface.

Detailed information could be found in Figure S23.

Author statement

Di Wei and Zhong Lin Wang: Proposed the idea and the whole project. **Di Wei, Lixue Yang, and Feiyang Yang:** Designed the experiment and performed the device fabrication and characterization. **Lixue Yang, Puguang Peng, and Han Qian:** Synthesized the samples. **Leo N. Y. Cao:** Performed the computational studies. **Lixue Yang:** Wrote the manuscript. **Di Wei and Shaoxin Li:** revised the manuscript. All the authors discussed the results and commented on the manuscript.

CRediT authorship contribution statement

Lixue Yang: Writing – review & editing, Writing – original draft, Methodology, Investigation, Formal analysis, Data curation, Conceptualization. **Leo N.Y. Cao:** Software. **Shaoxin Li:** Writing – review & editing. **Puguang Peng:** Methodology, Conceptualization. **Han Qian:** Data curation, Conceptualization. **Gehan Amaratunga:** Supervision, Investigation. **Feiyao Yang**: Methodology, Investigation. **Zhong Lin Wang**: Supervision, Investigation. **Di Wei:** Writing – review & editing, Supervision, Investigation.

Declaration of Competing Interest

The authors declare that they have no known competing financial interest or personal relationships that could have appeared to influence the work reported in this paper.

Data Availability

Data will be made available on request.

Acknowledgements

This work was supported by the Beijing Natural Science Foundation (Grant No. IS23040).

Appendix A. Supporting information

Supplementary data associated with this article can be found in the online version at doi:10.1016/j.nanoen.2024.110076.

References

[1] X. Zheng, G. Shen, C. Wang, Y. Li, D. Dunphy, T. Hasan, C.J. Brinker, B.-L. Su, Bio-inspired Murray materials for mass transfer and activity, Nat. Commun. 8 (2017) 14921, https://doi.org/10.1038/ncomms14921.

[2] M.W. Gaunt, M. Yeo, I.A. Frame, J.R. Stothard, H.J. Carrasco, M.C. Taylor, S. S. Mena, P. Veazey, G.A.J. Miles, N. Acosta, A.R. de Arias, M.A. Miles, Mechanism of genetic exchange in american trypanosomes, Nat 421 (2003) 936–939, https://doi.org/10.1038/nature01438.

[3] I.D. Couzin, J. Krause, N.R. Franks, S.A. Levin, Effective leadership and decision-making in animal groups on the move, Nat 433 (2005) 513–516, https://doi.org/10.1038/nature03236.

[4] R. Heidelberger, C. Heinemann, E. Neher, G. Matthews, Calcium dependence of the rate of exocytosis in a synaptic terminal, Nat 371 (1994) 513–515, https://doi.org/10.1038/371513a0.

[5] Z. Ding, Y. Wang, F. Chen, X. Hu, W. Cheng, Q. Lu, D.L. Kaplan, Biomimetic vascular grafts with circumferentially and axially oriented microporous structures for native blood vessel regeneration, Adv. Funct. Mater. 34 (2024) 2308888, https://doi.org/10.1002/adfm.202308888.

[6] H. Chen, F. Bian, L. Sun, D. Zhang, L. Shang, Y. Zhao, Hierarchically molecular imprinted porous particles for biomimetic kidney cleaning, Adv. Mater. 32 (2020) 2005394, https://doi.org/10.1002/adma.202005394.

[7] X.-Y. Yang, L.-H. Chen, Y. Li, J.C. Rooke, C. Sanchez, B.-L. Su, Hierarchically porous materials: synthesis strategies and structure design, Chem. Soc. Rev. 46 (2017) 481–558, https://doi.org/10.1039/C6CS00829A.

[8] G. Cai, P. Yan, L. Zhang, H.-C. Zhou, H.-L. Jiang, Metal–organic framework-based hierarchically porous materials: synthesis and applications, Chem. Rev. 121 (2021) 12278–12326, https://doi.org/10.1021/acs.chemrev.1c00243.

[9] M. Xia, D. Cai, J. Feng, P. Zhao, J. Li, R. Lv, G. Li, L. Yan, W. Huang, Y. Li, Z. Sui, M. Li, H. Wu, Y. Shen, J. Xiao, D. Wang, Q. Chen, Biomimetic hygroscopic fibrous membrane with hierarchically porous structure for rapid atmospheric water harvesting, Adv. Funct. Mater. 33 (2023) 2214813, https://doi.org/10.1002/adfm.202214813.

[10] K. Xiao, L. Jiang, M. Antonietti, Ion transport in nanofluidic devices for energy harvesting, Joule 3 (2019) 2364–2380, https://doi.org/10.1016/j.joule.2019.09.005.

[11] Y. Hu, J. Wei, Y. Liang, H. Zhang, X. Zhang, W. Shen, H. Wang, Zeolitic imidazolate framework/graphene oxide hybrid nanosheets as seeds for the growth of ultrathin molecular sieving membranes, Angew. Chem. Int. Ed. 55 (2016) 2048–2052, https://doi.org/10.1002/anie.201509213.

[12] Y. He, Y. Qiao, Z. Chang, H. Zhou, The potential of electrolyte filled MOF membranes as ionic sieves in rechargeable batteries, Energy Environ. Sci. 12 (2019) 2327–2344, https://doi.org/10.1039/C8EE03651A.

[13] Y. Guo, Y. Ying, Y. Mao, X. Peng, B. Chen, Polystyrene sulfonate threaded through a metal–organic framework membrane for fast and selective lithium-ion separation, Angew. Chem. Int. Ed. 55 (2016) 15120–15124, https://doi.org/10.1002/anie.201607329.

[14] Y.-C. Liu, L.-H. Yeh, M.-J. Zheng, K.C.-W. Wu, Highly selective and high-performance osmotic power generators in subnanochannel membranes enabled by metal-organic frameworks, Sci. Adv. 7 ((2021) eabe9924, https://doi.org/10.1126/sciadv.abe9924.

[15] Y. Liu, Y. Chen, Y. Guo, X. Wang, S. Ding, X. Sun, H. Wang, Y. Zhu, L. Jiang, Photo-controllable ion-gated metal–organic framework MIL-53 sub-nanochannels for efficient osmotic energy generation, ACS Nano 16 (2022) 16343–16352, https://doi.org/10.1021/acsnano.2c05498.

[16] B. Yao, S. Hussain, Z. Ye, X. Peng, Electrodeposited MOFs membrane with in situ incorporation of charged molecules for osmotic energy harvesting, Small 19 (2023) 2207559, https://doi.org/10.1002/smll.202207559.

[17] J. Xiao, M. Cong, M. Li, X. Zhang, Y. Zhang, X. Zhao, W. Lu, Z. Guo, X. Liang, G. Qing, Self-assembled nanoporous metal–organic framework monolayer film for osmotic energy harvesting, Adv. Funct. Mater. 34 (2024) 2307996, https://doi.org/10.1002/adfm.202307996.

[18] P. Peng, F. Yang, Z. Wang, D. Wei, Integratable paper-based iontronic power source for all-in-one disposable electronics, Adv. Energy Mater. 13 (2023) 2302360, https://doi.org/10.1002/aenm.202302360.

[19] T. Li, L. Yao, Q. Liu, J. Gu, R. Luo, J. Li, X. Yan, W. Wang, P. Liu, B. Chen, W. Zhang, W. Abbas, R. Naz, D. Zhang, Fluorine-free synthesis of high-purity Ti_3C_2T (T=OH, O) via alkali treatment, Angew. Chem. Int. Ed. 57 (2018) 6115–6119, https://doi.org/10.1002/anie.201800887.

[20] D. Wei, F. Yang, Z. Jiang, Z. Wang, Flexible iontronics based on 2D nanofluidic material, Nat. Commun. 13 (2022) 4965, https://doi.org/10.1038/s41467-022-32699-x.

[21] L. Yang, F. Yang, X. Liu, K. Li, Y. Zhou, Y. Wang, T. Yu, M. Zhong, X. Xu, L. Zhang, W. Shen, D. Wei, A moisture-enabled fully printable power source inspired by electric eels, PNAS 118 (2021) e2023164118, https://doi.org/10.1073/pnas.2023164118.

[22] X. Zheng, L. Niu, D. Wei, X. Li, S. Zhang, Label-free detection of microRNA based on coupling multiple isothermal amplification techniques, Sci. Rep. 6 (2016) 35982, https://doi.org/10.1038/srep35982.

[23] W. Zhao, Y. Wang, M. Han, J. Xu, L. Han, K.C. Tam, Osmotic energy generation with mechanically robust and oppositely charged cellulose nanocrystal intercalating GO membranes, Nano Energy 98 (2022) 107291, https://doi.org/10.1016/j.nanoen.2022.107291.

[24] J. Xia, H. Gao, S. Pan, T. Huang, L. Zhang, K. Sui, J. Gao, X. Liu, L. Jiang, Light-augmented multi-ion interaction in MXene membrane for simultaneous water treatment and osmotic power generation, ACS Nano 17 (2023) 25269–25278, https://doi.org/10.1021/acsnano.3c08487.

[25] S. Hong, J.K. El-Demellawi, Y. Lei, Z. Liu, F.A. Marzooqi, H.A. Arafat, H. N. Alshareef, Porous $Ti_3C_2T_x$ MXene membranes for highly efficient salinity gradient energy harvesting, ACS Nano 16 (2022) 792–800, https://doi.org/10.1021/acsnano.1c08347.

[26] G. Yang, Y. Qian, L. Wang, Y. Ma, J. Chen, H. Zang, X. Li, W. Lei, S. Qin, D. Liu, Advanced Janus membrane (MXene/CoAl-LDH) for efficient asymmetric ion transport and nanofluidic energy harvesting, Nano Energy 118 (2023) 108972, https://doi.org/10.1016/j.nanoen.2023.108972.

[27] X. Lin, P. Liu, W. Xin, Y. Teng, J. Chen, Y. Wu, Y. Zhao, X.-Y. Kong, L. Jiang, L. Wen, Heterogeneous MXene/PS-b-P2VP nanofluidic membranes with controllable ion transport for osmotic energy conversion, Adv. Funct. Mater. 31 (2021) 2105013, https://doi.org/10.1002/adfm.202105013.

[28] Q. Zhu, Y. Li, Q. Qian, P. Zuo, M.D. Guiver, Z. Yang, T. Xu, A sulfonated ultramicroporous membrane with selective ion transport enables osmotic energy extraction from multiform salt solutions with exceptional efficiency, Energy Environ. Sci. 15 (2022) 4148–4156, https://doi.org/10.1039/D2EE00851C.

[29] J. Zhou, J. Hao, R. Wu, L. Su, J. Wang, M. Qiu, B. Bao, C. Ning, C. Teng, Y. Zhou, L. Jiang, Maximizing ion permselectivity in MXene/MOF nanofluidic membranes for high-efficient blue energy generation, Adv. Funct. Mater. 32 (2022) 2209767, https://doi.org/10.1002/adfm.202209767.

[30] J. Lu, H. Xu, H. Yu, X. Hu, J. Xia, Y. Zhu, F. Wang, H.-A. Wu, L. Jiang, H. Wang, Ultrafast rectifying counter-directional transport of proton and metal ions in metal-organic framework–based nanochannels, Sci. Adv. 8 (2022) eabl5070, https://doi.org/10.1126/sciadv.abl5070.

[31] H. Zhao, Z. Xing, S. Su, S. Song, Z. Li, W. Zhou, Gear-shaped mesoporous NH_2-MIL-53(Al)/CdS P-N heterojunctions as efficient visible-light-driven photocatalysts, Appl. Catal. B: Environ. 291 (2021) 120106, https://doi.org/10.1016/j.apcatb.2021.120106.

[32] S.-W. Lv, J.-M. Liu, N. Zhao, C.-Y. Li, Z.-H. Wang, S. Wang, A novel cobalt doped MOF-based photocatalyst with great applicability as an efficient mediator of peroxydisulfate activation for enhanced degradation of organic pollutants, N. J. Chem. 44 (2020) 1245–1252, https://doi.org/10.1039/C9NJ05503G.

[33] X. Li, X. Ma, H. Zhang, N. Xue, Q. Yao, T. He, Y. Qu, J. Zhang, X. Tao, Ambient-stable MXene with superior performance suitable for widespread applications, Chem. Eng. J. 455 (2023) 140635, https://doi.org/10.1016/j.cej.2022.140635.

[34] Y. Zhou, H.-H. Chen, B. Yan, An Eu^{3+} post-functionalized nanosized metal–organic framework for cation exchange-based Fe^{3+}-sensing in an aqueous environment, J. Mater. Chem. A 2 (2014) 13691–13697, https://doi.org/10.1039/C4TA01297F.

[35] Z. Lu, Y. Wei, J. Deng, L. Ding, Z.-K. Li, H. Wang, Self-crosslinked MXene ($Ti_3C_2T_x$) membranes with good antiswelling property for monovalent metal ion exclusion, ACS Nano 13 (2019) 10535–10544, https://doi.org/10.1021/acsnano.9b04612.

[36] X. Ma, J. Tan, Z. Li, D. Huang, S. Xue, Y. Xu, H. Tao, Fabrication of stable MIL-53 (Al) for excellent removal of rhodamine B, Langmuir 38 (2022) 1158–1169, https://doi.org/10.1021/acs.langmuir.1c02836.

[37] M. Kim, S.M. Cohen, Discovery, development, and functionalization of Zr(iv)-based metal–organic frameworks, CrystEngComm 14 (2012) 4096–4104, https://doi.org/10.1039/C2CE06491J.

[38] S. Hong, F. Ming, Y. Shi, R. Li, I.S. Kim, C.Y. Tang, H.N. Alshareef, P. Wang, Two-dimensional $Ti_3C_2T_x$ MXene membranes as nanofluidic osmotic power generators, ACS Nano 13 (2019) 8917–8925, https://doi.org/10.1021/acsnano.9b02579.

[39] X. Sun, J. Yang, D. Su, C. Wang, G. Wang, Highly efficient adsorption of bilirubin by $Ti_3C_2T_x$ MXene, Chem. - Asian J. 16 (2021) 1949–1955, https://doi.org/10.1002/asia.202100332.

[40] M. Gao, M.-J. Zheng, A.F.M. El-Mahdy, C.-W. Chang, Y.-C. Su, W.-H. Hung, S.-W. Kuo, L.-H. Yeh, A bioinspired ionic diode membrane based on sub-2 nm covalent organic framework channels for ultrahigh osmotic energy generation, Nano Energy 105 (2023) 108007, https://doi.org/10.1016/j.nanoen.2022.108007.

[41] J. Feng, M. Graf, K. Liu, D. Ovchinnikov, D. Dumcenco, M. Heiranian, V. Nandigana, N.R. Aluru, A. Kis, A. Radenovic, Single-layer MoS_2 nanopores as nanopower generators, Nat 536 (2016) 197–200, https://doi.org/10.1038/nature18593.

[42] Z. Wu, T. Zhang, B. Wang, P. Ji, N. Sheng, M. Zhang, Q. Liang, S. Chen, H. Wang, Scalable bacterial cellulose biofilms with improved ion transport for high osmotic power generation, Nano Energy 88 (2021) 106275, https://doi.org/10.1016/j.nanoen.2021.106275.

[43] A.E. Khudozhitkov, S.S. Arzumanov, A.V. Toktarev, S.V. Cherepanova, A. A. Gabrienko, D.I. Kolokolov, A.G. Stepanov, Dissecting the effects of water guest adsorption and framework breathing on the $AlO_4(OH)_2$ centres of metal–organic framework MIL-53 (Al) by solid state NMR and structural analysis, Phys. Chem. Chem. Phys. 23 (2021) 18925–18929, https://doi.org/10.1039/D1CP03060D.

[44] J. Yang, B. Tu, G. Zhang, P. Liu, K. Hu, J. Wang, Z. Yan, Z. Huang, M. Fang, J. Hou, Q. Fang, X. Qiu, L. Li, Z. Tang, Advancing osmotic power generation by covalent organic framework monolayer, Nat. Nanotechnol. 17 (2022) 622–628, https://doi.org/10.1038/s41565-022-01110-7.

[45] Z. Zhang, X. Sui, P. Li, G. Xie, X.-Y. Kong, K. Xiao, L. Gao, L. Wen, L. Jiang, Ultrathin and ion-selective Janus membranes for high-performance osmotic energy conversion, J. Am. Chem. Soc. 139 (2017) 8905–8914, https://doi.org/10.1021/jacs.7b02794.

[46] J. Gao, W. Guo, D. Feng, H. Wang, D. Zhao, L. Jiang, High-performance ionic diode membrane for salinity gradient power generation, J. Am. Chem. Soc. 136 (2014) 12265–12272, https://doi.org/10.1021/ja503692z.

Lixue Yang is a master's student at Henan Normal University. She achieved the B.S. degree from Nanyang Normal University in 2020. Her research focuses on the transformation of ions and electrons, with applications in osmotic energy harvesting.

Prof. **Leo N.Y. Cao** received his Bachelor degree in Applied Mathematics from Xi'an Jiaotong University in 2008, Master degree in Environmental Management and Engineering in Hong Kong PolyU in 2010, and PhD degree in Mechanical Engineering in University of Minnesota in 2017. Now he is an associate professor in Beijing Institute of Nanoenergy and Nanosystems, Chinese Academic of Sciences. His main research interests are the applications of fluid dynamics and 3D printing on triboelectric nanogenerator, and science and technology of airborne charge particles.

Dr. Shaoxin Li is a post-doctor in the Beijing Institute of Nanoenergy and Nanosystems. She achieved the Ph.D degree from the University of Chinese Academy of Sciences in 2022 and the B.S. degree from the Jiangsu University in 2017. Her research interest is self-powered sensors, energy harvesting, and solid-liquid contact electrification.

Puguang Peng achieved the B.S. and M.S. degrees from the Xiangtan University in 2019 and 2022, respectively. He continues pursuing Ph.D. degree in Beijing Institute of Nanoenergy and Nanosystems, Chinese Academy of Sciences. He focuses on the transformation of ions and electrons, with the applications in iontronics, energy technology and intelligent sensing systems.

Han Qian is a master's student at University of Chinese Academy of Sciences. He achieved the B.S. degree from Henan University of Science and Technology in 2023. He focuses on the transformation of ions and electrons, with the applicatons in iontronics and osmotic energy harvesting.

Prof. Gehan Amaratunga received his B.Sc. degree in Electrical Engineering from the University of Wales, UK, and his Ph. D. from the University of Cambridge, UK, in 1983. Professor Amaratunga is a Fellow of the Institution of Electrical Engineers and a Chartered Engineer. In 2004, he was elected a Fellow of the Royal Academy of Engineering. In 2007, he was awarded the Royal Academy of Engineering's Silver Medal in recognition of his outstanding individual contribution to UK engineering. He is the founder, Chief Technology Officer, and Executive Director of Cambridge Semiconductor Ltd, a company specializing in power management integrated circuits. He has published over 500 academic papers in journals and conference proceedings, which have been cited more than 40,000 times, and he holds over 30 patents. Professor Amaratunga enjoys a high reputation in the industrial sectors of Europe, the United States, and Asia and has engaged in extensive technical and commercial collaborations with companies such as Philips and Ford.

Feiyao Yang is a senior engineer of Beijing Institute of Nanoenergy and Nanosystems, Chinese Academy of Sciences. He has working experience of more than ten years in the printing industry. His research interests are triboelectric nanogenerators, 2D nanofluidic materials, osmotic power source, printable electronics, and iontronics.

Prof. **Zhong Lin Wang** received his Ph.D. from Arizona State University in physics. He now is the Hightower Chair in Materials Science and Engineering, Regents' Professor, Engineering Distinguished Professor and Director, Center for Nanostructure Characterization, at Georgia Tech. Dr. Wang has made original and innovative contributions to the synthesis, discovery, characterization and understanding of fundamental physical properties of oxide nanobelts and nanowires, as well as applications of nanowires in energy sciences, electronics, optoelectronics and biological science. His discovery and breakthroughs in developing nanogenerators established the principle and technological road map for harvesting mechanical energy from environment and biological systems for powering personal electronics. His research on self-powered nanosystems has inspired the worldwide effort in academia and industry for studying energy for micro-nano-systems, which is now a distinct disciplinary in energy research and future sensor networks. He coined and pioneered the field of piezotronics and piezophototronics by introducing piezoelectric potential gated charge transport process in fabricating new electronic and optoelectronic devices. Details can be found at: http://www.nanoscience.gatech.edu.

Prof. **Di Wei** serves as the Principal Investigator at BINN and heads the Iontronics Laboratory. As Fellow of the Royal Society of Chemistry (FRSC) and Senior Member of Wolfson College at Cambridge University, he has published over 100 papers including Nature Energy, Nature Commun., PNAS, Adv Mater, Energ Environ Sci., Matter etc. as the first/corresponding author. Prof. Wei also has a portfolio of over 200 international patents (including PCT). Notably, 92 patents have been successfully granted, many of which have been transferred to leading companies like Nokia in Finland and Lyten in the USA. Additionally, Prof. Wei has edited 3 English books, published by Wiley and Cambridge University Press etc., focusing on nanotechnology for energy and information technology. His achievements have been recognized by the first prize of the Nokia Global Innovation and Excellence Award, Brian Conway Prize in Physical Electrochemistry from the International Society of Electrochemistry (ISE) and various other prizes from ISE and RSC. Details can be found at: http://iontronics.group/en/